



CHORUS

This is the accepted manuscript made available via CHORUS. The article has been published as:

Particle-bubble interaction inside a Hele-Shaw cell

Peng Zhang, John M. Mines, Sungyon Lee, and Sunghwan Jung

Phys. Rev. E **94**, 023112 — Published 22 August 2016

DOI: [10.1103/PhysRevE.94.023112](https://doi.org/10.1103/PhysRevE.94.023112)

Particle-bubble interaction inside a Hele-Shaw cell

Peng Zhang¹, John M. Mines¹, Sungyon Lee^{2,*} and Sunghwan Jung^{1†}

¹ *Department of Biomedical Engineering and Mechanics, Virginia Tech, Blacksburg, VA 24061, USA and*

² *Mechanical Engineering, Texas A&M University, College Station, TX 77843, USA*

(Dated: July 29, 2016)

Hydrodynamic interactions between air bubbles and particles have wide applications in multiphase separation and reaction processes. In the present work, we explore the fundamental mechanism of such complex processes by studying the collision of a single bubble with a fixed solid particle inside a Hele-Shaw cell. Physical experiments show that an air bubble either splits or slides around the particle depending on the initial transverse distance between the bubble and particle centroids. An air bubble splits into two daughter bubbles at small transverse distances, and slides around the particle at large distances. In order to predict the critical transverse distance that separates these two behaviors, we also develop a theoretical model by estimating the rate of the bubble volume transfer from one side of the particle to the other based on Darcy's law, which is in good agreement with experiments.

I. INTRODUCTION

Hydrodynamic interactions between rigid particles and bubbles are a topic of fundamental interest in fluid mechanics and are central in numerous industrial applications. For instance, the success of mineral flotation critically hinges on the collision, attachment, and detachment of particles with bubbles in a suspension [1]. There exist a number of limited theories describing the collision efficiency between particles and a rising bubble (i.e. see [2] for review), as well as experimental work involving particle-bubble interactions in a turbulent flow [3–5] or a single bubble collecting particles [6]. In the context of microfluidics, acoustic bubbles are used to trap and sort micro-particles [7, 8], based on acoustically actuated streaming flows [9] or secondary radiation forces [10]. Regardless of the specific application, the central focus of the aforementioned studies is the dynamics of the rigid particles in the presence of a bubble. In particular, in systematic experiments both in flotation and acoustofluidics, the bubble is considered a static element whose location and shape are fixed or externally controlled.

Distinct from the previous work on the particle-bubble interactions, we presently focus on the dynamics of a freely rising and evolving bubble around a fixed particle. We hereby adopt the experimental and theoretical approach typically used in the fundamental study of drops and bubbles. The dynamics of bubbles and drops has been extensively studied particularly inside the Hele-Shaw cell, which allows for greater visualization and controllability [11–13]. For instance, Maxworthy et al. [14] observed complex interactions between multiple air bub-

bles in a Hele-Shaw cell, including merging and break-up of bubbles as similarly observed in [15–17].

While the bubble or drop break-up can be induced by capillary forces under shear [18], geometrical obstacles have also been introduced in the microfluidic channels as means to induce and control droplet break-ups [19–21]. Link et al. [19] conducted systematic experiments of droplet breakup due to geometric obstacles; this phenomenon was later theoretically resolved based on a one-dimensional Darcy flow [20]. In particular, a threshold capillary number, Ca , (ratio of viscous forces to interfacial tension) for drop break-up was obtained based on the simple model and used to generate and control the daughter droplet sizes in microfluidic channels. More recently, Salkin et al. [22, 23] modeled an analogous problem by estimating the pressure drop along the microfluidic channel. The critical capillary number that separates the break-up and sliding phenomena was predicted, which showed good agreement with the experimental data.

In this paper, we examine the interaction between a fixed particle and a rising bubble in a Hele-Shaw cell, in a flow configuration that has not been previously considered. We perform experiments in the regions of high Bond number, Bo , and low capillary number, Ca , so that gravity and surface tension are dominant forces in the system. The experimental setup and methods are detailed in Sec. II. Bubble morphologies during the interaction with the particle are recorded and analyzed with image processing tools, which yields the bubble volume and the position of the bubble centroid for all experimental runs. In particular, the rising bubble is observed to either *slide* around the particle or *split* into two daughter bubbles, depending on the transverse distance between the bubble and particle centroids, as shown in Sec. III A. This transitional behavior of the bubble from sliding to splitting is analogous to that of the droplet from sliding to break-up in the 1-D channel experiments [20]. The

* sungyon.lee@tamu.edu

† sunnyjsh@vt.edu

experimental results are then rationalized by considering the Darcy flow in the liquid phase around the evolving bubble as it interacts with the fixed particle in Sec. III B.

II. EXPERIMENTAL SETUP

In this study, we focus on the dynamics of a single air bubble rising in the presence of a fixed particle inside a Hele-Shaw cell. The two-dimensional channel consists of two $20 \times 25 \text{ cm}^2$ glass plates separated by a gap of $h = 1.5 \text{ mm}$. A spherical steel particle of 1.2 mm in diameter is attached to the plate with a small amount of adhesive glue prior to the experiment (Fig. 1(a)), so that it spans the cell gap thickness. The Hele-Shaw cell is filled with a glycerin solution (CAS# 56-81-5, PTI Process Chemicals) mixed with water to reach the approximate concentration of 90% by weight for all experiments. The surface tension of the solution is measured to be $\gamma = 61.99 \pm 0.04 \text{ mN/m}$ in a tensiometer (KRUSS Force Tensiometer K11), and its dynamic viscosity is $\mu = 238.01 \pm 2.50 \text{ mPa}\cdot\text{s}$, based on viscometer measurements (Vibro Viscometer, A&D Company Ltd).

In the experiments of over 180 trials, a single air bubble is injected into a quiescent glycerin solution from the bottom of the Hele-Shaw cell by a syringe and rises under the action of buoyancy. The vertical distance between the fixed particle and the bottom of the Hele-Shaw cell is large enough ($\sim 15 \text{ cm}$) to ensure that the bubble reaches the terminal velocity before interacting with the particle. A thin fluid film is observed to be always present between the air bubble and the Hele-Shaw cell walls in the experiments. A Nikon D7000 video camera is mounted in front of the Hele-Shaw cell to record the air bubble dynamics with 1280×720 pixel images at 23 frames per second. The resolution of the recorded images is given by 0.072 mm/pixel . At each frame, the edge of an evolving air bubble is detected using the MATLAB image processing toolbox, from which the bubble volume, centroid, curvature, and velocity can be computed for further analysis.

In our analysis, a Cartesian coordinate system is defined with the origin located at the center of the fixed particle, as illustrated in Fig. 1(a); the fluid motion normal to the Hele-Shaw wall (or z -direction) is neglected in the current study. In the experiments, large freely rising bubbles ($R > 1.0 \text{ cm}$) become unstable and split into daughter bubbles even in the absence of the particle. On the other hand, small bubbles ($R < 0.30 \text{ cm}$) are stable and exhibit only minimal deformations against the particle without splitting. Therefore, the air bubble radius is chosen to be between 0.50 and 0.75 cm to ensure that the bubble rises stably and exhibits the transition from sliding to splitting under various flow conditions. Since

the bubble diameter is consistently larger than the particle diameter (1.2 mm), the effects of the finite particle size on the deforming bubble shape will not be considered in our model presented in Sec. III B. The transverse distance between the particle and bubble centroid positions along the x -direction is measured and denoted as d (Fig. 1(a)). The value of d (ranging from 0 to 2.5 mm) is adjusted by shifting the position of the particle incrementally between experimental runs. The capillary number ($Ca = \mu U / \gamma$, where U is the free-rising velocity of the bubble) is in the range of 0.043 to 0.054 , while the Bond number, $Bo = \rho g R^2 / \gamma$, varies between 4.7 and 11.0 , where $\rho = \rho_{\text{fluid}} - \rho_{\text{air}} \approx 1.20 \text{ g/cm}^3$ is the density difference, and g is the gravitational acceleration.

III. RESULTS

A. Experimental Results

Three representative bubble behaviors are observed for varying values of the transverse distance, d , as shown in Fig. 1(b) [24]. For small d values ($d < 0.2 \text{ mm}$), upon coming into contact with the particle, the air bubble deforms and splits into two daughter bubbles on both sides of the particle (Fig. 1(b-*i, ii*)); for large d values ($d > 1.0 \text{ mm}$), the bubble deforms and slides around the particle (Fig. 1(b-*iii*)). Equal and unequal daughter bubbles are observed in the former case. Corresponding to the low Ca limit, air bubble shapes are stable upstream of the particle, and the sliding bubbles always tend to restore their original shapes downstream. The extracted bubble shapes and centroid positions corresponding to cases (*i*)-(*iii*) are shown in Fig. 2(a). In addition, we compute the curvature of the boundary on the x - y plane as

$$\kappa_{\text{exp}} = \frac{x'y'' - y'x''}{(x'^2 + y'^2)^{3/2}}, \quad (1)$$

where $x(s)$ and $y(s)$ denote the position of the bubble boundary in the horizontal and vertical directions, respectively, while s is the coordinate defined along the boundary. The derivatives in Eq. (1) are computed by a central difference scheme. A B-form spline function is used to smooth the x and y coordinates of the boundary before the derivatives are calculated [25]. An example of the in-plane boundary curvature is shown in Fig. 2(b).

In our analysis, we track the bubble volume from each frame, which is equivalent to the projected bubble area (A) on the x - y plane. Specifically, we consider the bubble area on the left and right sides of the particle, i.e., A_l and A_r , respectively, which yields the area difference, $\Delta A(t) = A_r(t) - A_l(t)$. The normalized area difference

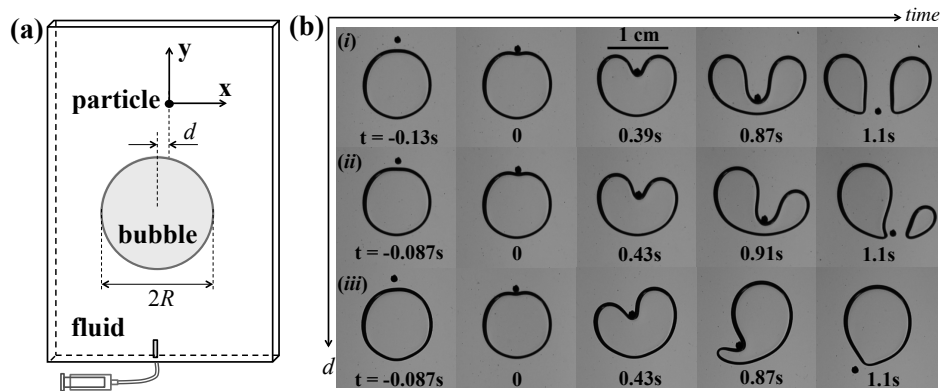


FIG. 1. (a) Schematic of the experimental setup with key parameters and the coordinate system. (b) The image sequence from three representative experiments demonstrating the interaction of the bubble and a fixed particle: (i) equal splitting, (ii) unequal splitting, and (iii) sliding bubbles. The bubble diameter ($2R$) in (i)-(iii) corresponds to 1.187, 1.183 and 1.184 cm, while the values of the transverse distance between the particle and bubble centroids, d , are 0.03, 0.16 and 0.51 mm, respectively.

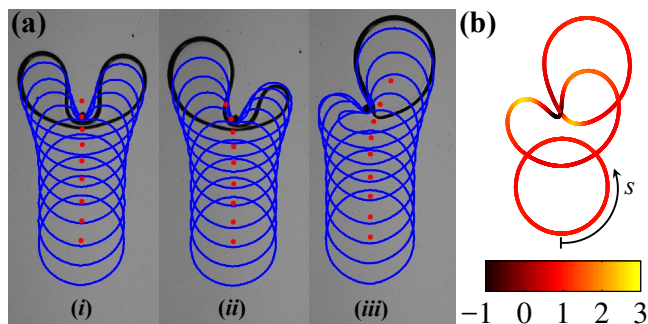


FIG. 2. (Color online) (a) The evolving boundaries and centroid positions of the bubbles corresponding to cases (i)-(iii) shown in Fig. 1(b). (b) The in-plane boundary curvature ($R\kappa_{\text{exp}}$) of case (iii) at three different frames. Here s denotes the coordinate defined along the bubble boundary.

curves $|\Delta A/A|$ are plotted as a function of time in Fig. 3, which represents the bubble volume shift from one side of the particle to the other. The $|\Delta A/A|$ curves clearly exhibit a transition between splitting and sliding bubbles. For sliding bubbles, the volume on one side of the particle completely migrates to the other, so that the value of $|\Delta A/A|$ must reach one before some final time. For splitting bubbles, on the other hand, the two sides of the bubble do not completely merge; hence, the value of $|\Delta A/A|$ remains strictly less than one for all times. Notably, we observe that the overall behavior of $|\Delta A/A|$ strongly depends on its initial value at $t \sim 0$, i.e. the initial transverse distance, d . Based on this key observation, we develop a reduced theoretical model that computes

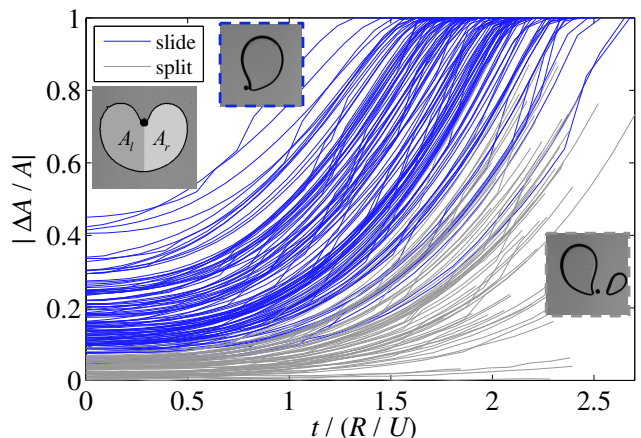


FIG. 3. (Color online) The normalized area difference, $|(A_r - A_l)/A|$, is plotted as a function of the dimensionless time, $t/(R/U)$ for all different values of d . The dark blue lines correspond to the sliding bubbles, while the light gray lines are the splitting bubbles.

the evolution of $|\Delta A/A|$. This model allows us to predict the critical transverse distance d_c that separates the splitting and sliding behaviors in the following section.

B. Theoretical Model

In this section, we propose a theoretical model to predict the bubble volume shift between the two sides of the bubble separated by the fixed particle. We focus on the

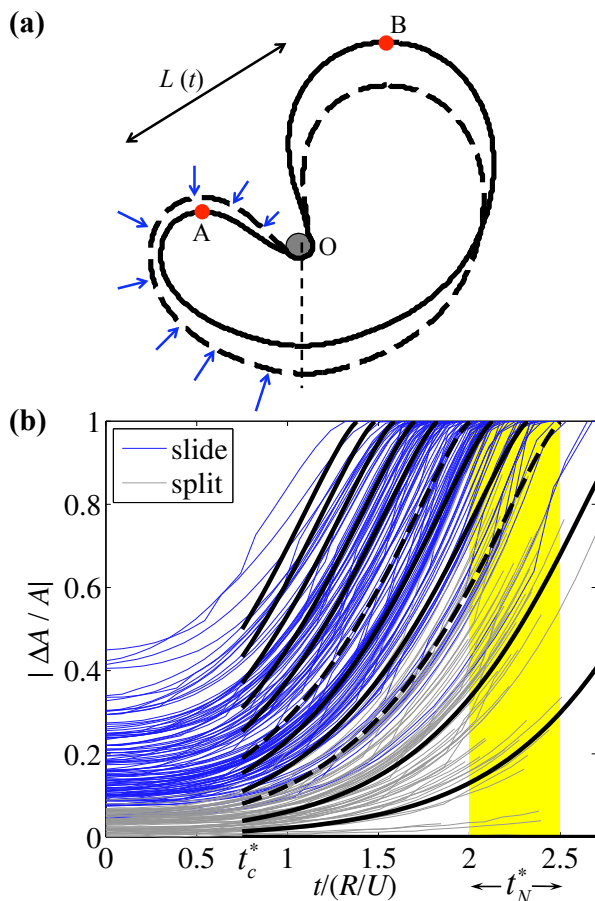


FIG. 4. (Color online) (a) Deformed bubble shapes at two different instants during the bubble-particle interaction process. (b) Modeled bubble area shift with a range of initial $\Delta A/A$ values, compared with experiment data shown in Fig. 3. Parameters $\bar{\alpha} = 0.8$ and $\bar{\beta} = 0.75$ are used in the model (Eq. (4)). The critical time $t_c^* = 0.75$ is assumed in this figure. Corresponding to the final time $t_N^* = 2$ and 2.5 , the predicted transition curves that separate the sliding and splitting cases are shown as dashed curves.

fluid motion around the bubble with a highly deformed shape as shown in Fig. 4(a) that contain snapshots of two successive bubble shapes of case (iii). The fluid motion on the boundary of the left side of the bubble is denoted by arrows. Based on our observations, the fluid motion can push the air from the left to the right side of the particle, and thus shrink the volume of the left side of the bubble (Appendix A). The shrinking rate of the air volume can be estimated by the fluid velocity (\mathbf{u}) and the length of the left-hand side of the bubble (S_l) as

$$\frac{d(A_l h)}{dt} \sim -|\mathbf{u}|S_l h. \quad (2)$$

Instead of computing the exact value of \mathbf{u} everywhere on the boundary, we estimate the order of magnitude of \mathbf{u} based on the fluid pressure. According to Darcy's law [11], the fluid velocity in a Hele-Shaw cell is related to the fluid pressure gradient as

$$\nabla p' = \nabla(p + \rho g y) = -\frac{1}{c} \mathbf{u}, \quad (3)$$

where constant $c = h^2/12\mu$, and the modified pressure is $p' = p + \rho g y$. The pressure gradient $\nabla p'$ is estimated by the boundary curvature of a deformed bubble; then the rate of change in the left-bubble volume is computed by Eq. (2).

Without loss of generality, let us assume $A_l \leq A_r$ in the following discussions. If we non-dimensionalize all variables by the free-rising velocity of the bubble $U = \rho g h^2/12\mu$ [11, 26], the bubble radius R before deformation, the characteristic time $T = R/U$ and the total projected area $A = \pi R^2$, the shrinking rate of the bubble projected area of the left side can be expressed as

$$\frac{dA_l^*}{dt^*} = -\bar{\beta} \left(\frac{\bar{\alpha}}{Bo\sqrt{A_l^* A_r^*}} + \pi \right) \frac{\sqrt{A_l^*}(\sqrt{A_r^*} - \sqrt{A_l^*})}{\sqrt{A_r^*} + \sqrt{A_l^*}}, \quad (4)$$

with dimensionless variables denoted as $(\cdot)^*$, $A_r^* = 1 - A_l^*$ and $A_l^* \leq 0.5$. Parameter $\bar{\alpha}$ is determined by the geometry of the bubble and $\bar{\beta}$ is a free parameter. Experimentally, we find $\bar{\alpha} \approx 0.8$. The detailed derivation of Eq. (4) and the physical meaning of $\bar{\alpha}$ and $\bar{\beta}$ are provided in Appendix B.

When we calculate the flow velocity in Eq. (3), the estimated pressure gradient $\nabla p'$ is valid only for bubbles that have undergone large deformations. In other words, Eq. (4) does not hold prior to or in the initial stage of the interaction between the bubble and particle. Thus, we define a critical time, t_c^* , at which the bubble volume starts to shift from one side of the particle to the other, and assume that Eq. (4) is valid for $t \geq t_c^*$. We find that with the measured value of $\bar{\alpha} = 0.8$ and the free parameter $\bar{\beta} = 0.75$, the volume shift predicted by our model (Eq. (4)) matches the experimental data, as shown in Fig. 4(b).

As discussed in Sec. III A, the transition between splitting and sliding bubbles can be predicted by the value of $|\Delta A(t^*)/A|$ at a later time, t_N^* . Here, t_N^* is defined as the moment at which the bottom of the bubble rises to the particle. For the sliding case, the bubble slides around the particle by shifting the volume from one side of the particle to the other before t_N^* . For example, in Fig. 4(b), the value of $|\Delta A(t^*)/A|$ for sliding bubbles becomes one before the final time, t_N^* . For splitting bubbles, the volume transfer process is slower; therefore, the

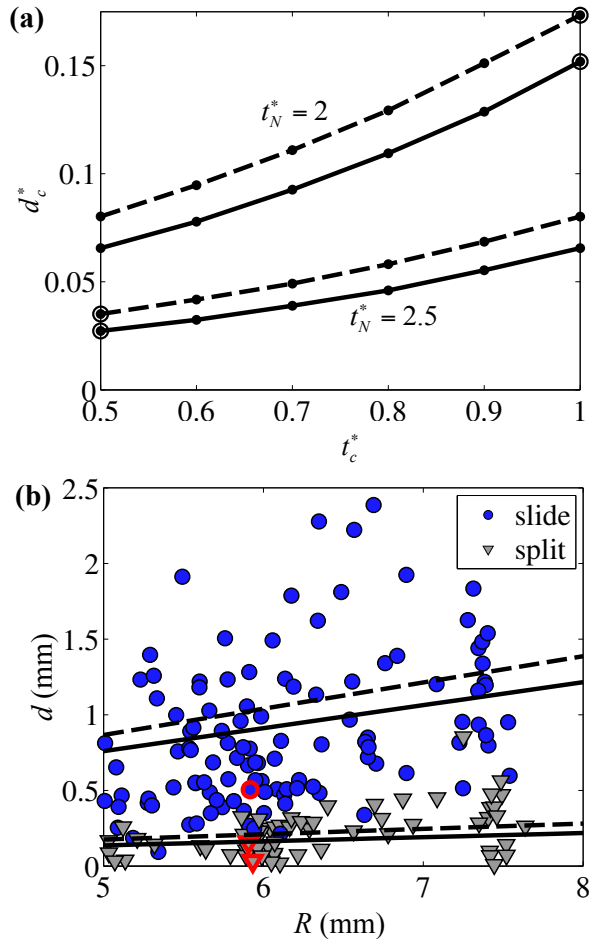


FIG. 5. (Color online) (a) The critical transition d_c^* predicted by our model for different t_c^* and t_N^* values. (b) The d - R phase diagram that exhibits the transition between sliding and splitting bubbles. The blue circles correspond to sliding bubbles, while the gray upside-down triangles indicate splitting bubbles. The predicted minimum and maximum values of this transition are $d_c^* = 0.027$ & $d_c^* = 0.151$ for $R = 5$ mm (solid lines) and $d_c^* = 0.035$ & $d_c^* = 0.173$ for $R = 7.5$ mm (dashed lines). The three representative cases (i)-(iii) are labeled with red edges.

value of $|\Delta A(t^*)/A|$ remains below one even at $t = t_N^*$. Based on this criterion, for a given transverse distance, d^* , we can determine the bubble behavior by computing the value of $|\Delta A(t_N^*)/A|$. The final time t_N^* in this problem is expected to satisfy $t_N^* \geq 2$, due to the fact that the interaction with the particle slows down the rising speed of the bubble. Therefore, in our prediction of d_c^* we choose $2 \leq t_N^* \leq 2.5$. With a range of critical time $0.5 \leq t_c^* \leq 1$, the predicted critical transverse distance d_c^* is shown in Fig. 5(a). Finally, the predicted transition

between splitting and sliding bubbles with the maximum and minimum d_c^* values are plotted as solid black lines in Fig. 5(b), which captures the sliding-splitting transition regime observed in the experiments.

The Bond number (Bo) in Eq. (4) is estimated based on the smallest bubble size ($R = 0.5$ cm), and the minimum and maximum critical transverse distances ($d_c^* = 0.027$ & 0.151) are calculated. To check the sensitivity of the choice of R , we repeat the calculations with the largest bubble size ($R = 0.75$ cm) as shown in dashed lines in Fig. 5(a,b). We find that the minimum and maximum critical transverse distances are $d_c^* = 0.035$ and $d_c^* = 0.173$ respectively, which corresponds to a 26% increase in d_c^* while R is increased by 40% and does not affect the overall trend.

IV. CONCLUSION

In this paper, we investigate the interaction between a single air bubble and a fixed particle in a quasi-two-dimensional domain created by a Hele-Shaw cell. In the limit of high Bond and low capillary numbers, the resultant behavior of the bubble upon interacting with the particle solely depends on the initial transverse distance between the bubble and particle centroids. Experimentally, the interaction between the bubble and the particle is recorded with a camera, and the time-dependent bubble morphologies are extracted with image processing tools. We observe that the bubble slides around the particle for small values of the transverse distance, d , while it breaks up into daughter bubbles for large d . The critical transverse distance, d_c , at which the bubble transitions from sliding to splitting is experimentally measured.

In order to model the transition between the splitting and sliding bubbles, we use Darcy's equation to estimate the magnitude of the fluid velocity associated with a deforming bubble in the Hele-Shaw cell. This velocity estimate is used to predict the rate of bubble volume shift from the smaller to the larger side, which agrees well with the experimental measurements. Based on the plot of the bubble volume shift, we observe that the overall bubble dynamics strongly depends on the bubble configuration at early times. By assuming that the bubble volume transfer starts from some critical time, t_c , this model leads to the prediction of the critical transverse distance, d_c , that separates the splitting and sliding cases.

Our experiments are performed at low Ca and high Bo , so that buoyancy and surface tension forces are dominant over viscous effects. Thus, equation (4) describing the bubble-area shift is derived from a balance between these two dominant effects, determined solely by the value of Bo and independent of Ca . As long as Ca is low, a change in Ca (e.g. changes in the fluid viscosity and the gap

thickness) will affect the characteristic time scale ($T = R/U; U \simeq \rho gh^2/12\mu$) but have no significant impact on the overall dynamics that follows Eq. (4). Furthermore, if Ca becomes greater than 1, the buoyancy and viscous forces become dominant, and bubble dynamics would be quite different from our work presented here, which is outside of the scope of our study.

The current work provides an integrated experimental and theoretical framework to rationalize the air bubble and particle interactions in a quasi-two-dimensional fluid domain. The results can be potentially extended to systems with liquid droplets. Specifically, the model on the bubble volume shift may prove useful for industrial processes, in which gravity-driven bubbles past geometric obstacles are employed to generate controllable bubble sizes.

ACKNOWLEDGMENTS

Acknowledgment is made to the donors of the American Chemical Society Petroleum Research Fund, the National Science Foundation (CBET-1336038), and VT-ICTAS for partial support of this research.

Appendix A: Flow field around a deforming bubble

The flow field around a deforming air bubble can be obtained from the pressure field using the relation in Eq. (3). The modified pressure field (p') of the fluid in a Hele-Shaw cell satisfies the two-dimensional Laplace equation

$$\nabla^2 p' = 0. \quad (\text{A1})$$

The Laplace equation above can be solved numerically by the boundary element method (BEM). The solution to Eq. (A1) can be expressed as

$$p'(\mathbf{x}_0) = -c \int_S G(\mathbf{x}, \mathbf{x}_0) (\mathbf{n} \cdot \nabla p'(\mathbf{x})) dS(\mathbf{x}) \quad (\text{A2}) \\ + c \int_S p'(\mathbf{x}) (\mathbf{n} \cdot \nabla G(\mathbf{x}, \mathbf{x}_0)) dS(\mathbf{x}),$$

where S denotes the boundary of the bubble in the x - y plane. Here, the constant $c = 1$ when \mathbf{x}_0 is located in the fluid and $c = 2$ when \mathbf{x}_0 is on the boundary. The Green's function (G) is defined as $G(\mathbf{x}, \mathbf{x}_0) = -\ln|\mathbf{x} - \mathbf{x}_0|/(2\pi)$. Experimentally, the normal velocity of the bubble boundary, $\mathbf{u}_n = \mathbf{n} \cdot \nabla p'(\mathbf{x})$ (refer to Eq. (3)), can be measured from bubble boundary shapes on successive frames as shown in Fig. 4(a). Using this measured velocity as the

boundary condition, the modified pressure on the boundary of the bubble and in the fluid can then be solved numerically based on Eq. (A2).

The pressure (p' and p) and velocity (\mathbf{u}) field distributions around the bubble are computed from Eq. (A2) and Eq. (3). The computed pressure field and velocity field are shown in Fig. 6 and Fig. 7, respectively. The velocity distribution verifies our assumption that the air volume shifts from the large to the small side as the bubble deforms.

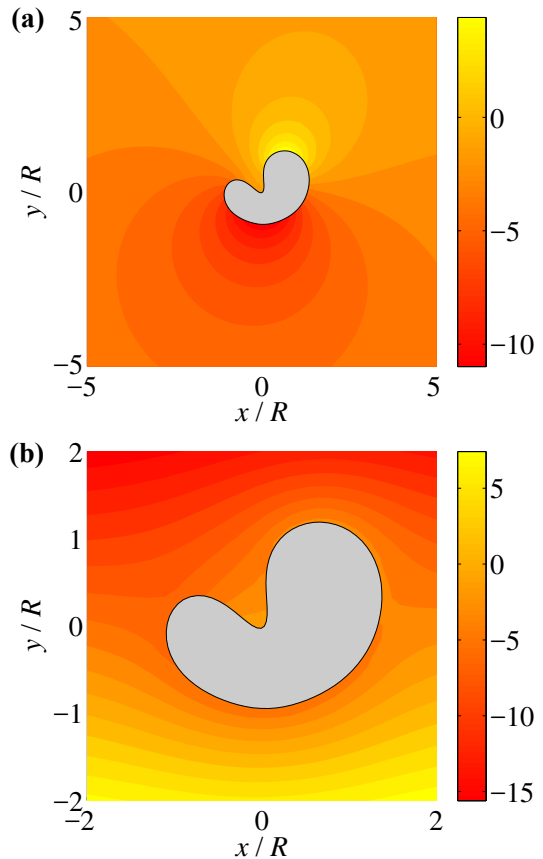


FIG. 6. (Color online) The BEM simulation results for (a) $p'/(σ/R)$ and (b) $p/(σ/R)$ distribution around a deforming bubble.

Appendix B: Derivation of the theoretical model

In order to model the velocity in Eq. (3), we need to obtain the expression for the pressure difference, Δp , and the relative vertical position, Δy , between the left and right sides of the deformed bubble. First, we assume the pressure inside the bubble is constant as $p = p_0$, while the pressure outside the bubble boundary can be derived

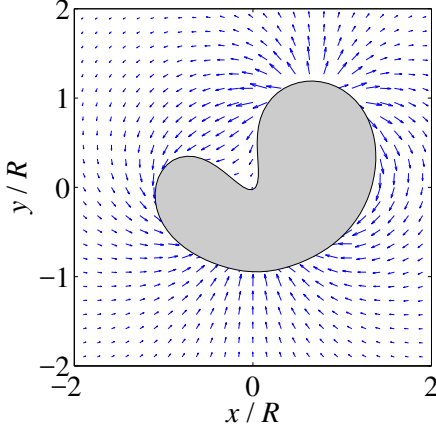


FIG. 7. (Color online) The velocity field derived from the numerically computed pressure field using Eq. (3).

from the Young-Laplace equation: $p = p_0 - \sigma\kappa$ [11, 27]. Here, the curvature (κ) is the sum of the in-plane (κ^{xy}) and out-of-plane ($\kappa^z = 2/h$) curvatures, i.e., $\kappa = \kappa^{xy} + \kappa^z$. We postulate that the curvature of the deformed bubble on either side of the particle is related to its area (A) by

$$\kappa^{xy} = \frac{\alpha_1}{\sqrt{A}}, \quad (\text{B1})$$

where α_1 is a parameter for the curvature estimates. Note that the curvature in Eq. (B1) represents an estimate of an average curvature of either side of the bubble, rather than a local curvature along the boundary.

In the following calculation, we still retain the assumption that $A_l \leq A_r$. From Eq. (B1), the curvature difference between the two sides is given by

$$\Delta\kappa = \kappa_r^{xy} - \kappa_l^{xy} = \alpha_1(A_r^{-1/2} - A_l^{-1/2}). \quad (\text{B2})$$

To validate the above equation, we experimentally measure the relation between the curvature and the projected bubble area; here, the curvature of the evolving bubble is calculated using Eq. (1). To estimate the average curvature in Eq. (B1), we take the arc-length averaged value of the curvature, such that

$$\kappa^{xy} \approx \bar{\kappa}^{xy} = \frac{\int_s \kappa_{\text{exp}} ds}{\int_s ds}. \quad (\text{B3})$$

Figure 8(a) shows the relation between the measured dimensionless curvature difference $R\Delta\kappa \approx R(\bar{\kappa}_r^{xy} - \bar{\kappa}_l^{xy})$ and $R(1/\sqrt{A_r} - 1/\sqrt{A_l})$ values, which indicates a linear relation with the slope $\alpha_1 \approx 1.2$. In the case of a semi-circular bubble (as a rough approximation of the bubbles in experiments), the in-plane curvature is given

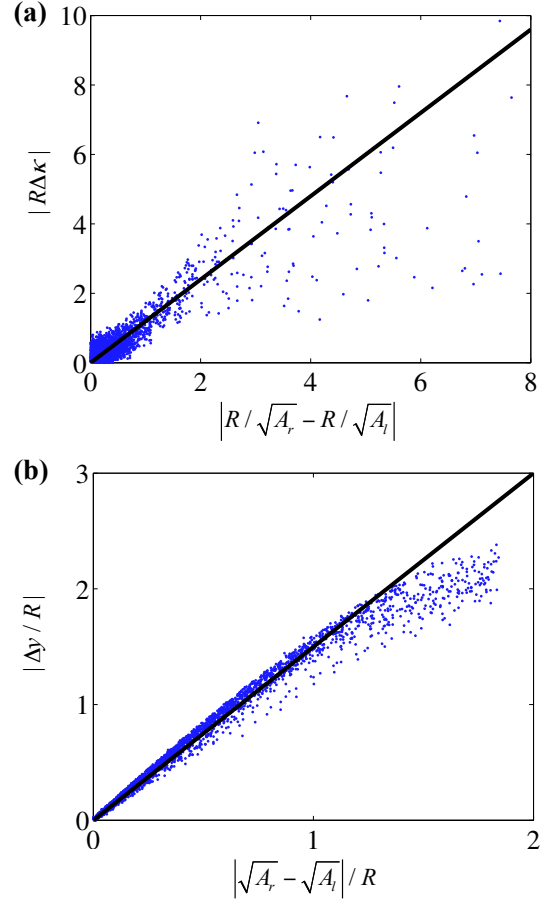


FIG. 8. (Color online) (a) The curvature difference $|\Delta\kappa|$ as a function of $|1/\sqrt{A_l} - 1/\sqrt{A_r}|$ based on measurement (blue dots). The black line has a slope of 1.2. (b) The measured vertical distance $|\Delta y|$ as a function of $|\sqrt{A_r} - \sqrt{A_l}|$ (blue dots). The black line has a slope of 1.5. In both plots, x - and y -axes are normalized by the length scale R .

as $\kappa^{xy} = \sqrt{\pi/(2A)}$ corresponding to $\alpha_1 \approx 1.3$, which is close to the measured value.

The relative vertical position ($\Delta y = y_r - y_l$) between the right and left bubble sides is assumed to be proportional to the square-root of their area

$$\Delta y = y_r - y_l = \alpha_2(\sqrt{A_r} - \sqrt{A_l}), \quad (\text{B4})$$

where α_2 is another parameter introduced to correlate the area difference to the height difference. From our experiments, Δy is estimated from the vertical distance between the apexes of both sides (i.e., points “A” and “B” in Fig. 4), $\Delta y \approx y_B - y_A$, and the relation between Δy and $(\sqrt{A_r} - \sqrt{A_l})$ is shown in Fig. 8(b). The linear relation assumed in Eq. (B4) is supported with $\alpha_2 \approx 1.5$. Again, in the case of two semi-circular bubbles attached,

the height difference becomes $\Delta y = \sqrt{2/\pi}(\sqrt{A_r} - \sqrt{A_l})$ corresponding to $\alpha_2 \approx 0.8$, which is on the same order of magnitude as the measured value. The difference in the values is primarily due to a very rough approximation of assuming two semi-circular shapes for a deformed bubble.

Finally, the pressure difference between the two sides is expressed as

$$\Delta p' = (p + \rho g y)_r - (p + \rho g y)_l = -\sigma\alpha_1(A_r^{-1/2} - A_l^{-1/2}) + \alpha_2\rho g(\sqrt{A_r} - \sqrt{A_l}). \quad (\text{B5})$$

In order to compute the pressure gradient that drives the fluid flow from the right to the left side of the particle, we define a length scale associated with the flow between the two sides, L , as shown in Fig. 4(a). With the introduction of another geometric parameter α_3 , we estimate L as $L = \alpha_3(\sqrt{A_r} + \sqrt{A_l})$. The magnitude of fluid velocity (u) can now be approximated as

$$u \approx -c \frac{\Delta p'}{L} = -\frac{c}{\alpha_3} \left(\frac{2\alpha_1\sigma}{\sqrt{A_l A_r}} + \alpha_2\rho g \right) \frac{\sqrt{A_r} - \sqrt{A_l}}{\sqrt{A_r} + \sqrt{A_l}}. \quad (\text{B6})$$

The bubble shrinking rate Eq. (2) can then be expressed more precisely as

$$\frac{dA_l}{dt} = -\beta|u|S_l, \quad (\text{B7})$$

where β is a modification parameter for the flow rate. Note that Eqs. (B6, B7) are not valid if the fixed particle is large enough to block the liquid flow between the left and right bubble sides. The size effect of the solid particle is neglected here because the particle is small compared to the size of the air bubbles. If we model the left side boundary length S_l as $S_l = \alpha_4\sqrt{A_l}$, where α_4 is another geometric parameter, Eq. (B7) becomes

$$\frac{dA_l}{dt} = -\left(\beta \frac{\alpha_4}{\alpha_3}\right) \frac{h^2}{12\mu} \left(\frac{\alpha_1\sigma}{\sqrt{A_l A_r}} + \alpha_2\rho g \right) \times \frac{\sqrt{A_l}(\sqrt{A_r} - \sqrt{A_l})}{\sqrt{A_r} + \sqrt{A_l}}. \quad (\text{B8})$$

In the above analyses, the parameters $\alpha_1, \alpha_2, \dots, \alpha_4$ and β are introduced as parameters for the order of magnitude estimate of length scales and flow rate. By redefining the parameters as $\bar{\alpha} = \alpha_1/\alpha_2$ and $\beta = \beta\alpha_2\alpha_4/\pi^{3/2}\alpha_3$, Eq. (4) is obtained. The experimental measurements of α_1 and α_2 yield $\bar{\alpha} \approx 0.8$.

-
- [1] A. Nguyen and H. Schulze, Colloidal science of flotation (Marcel Dekker, New York, 2004).
 - [2] Z. Dai, D. Fornasiero, and J. Ralston, *Advances in Colloid and Interface Science* **85**, 231 (2000).
 - [3] R. Yoon and G. Luttrell, *Mineral Processing and Extractive Metallurgy Review* **5**, 101 (1989).
 - [4] H. Schulze, *Mineral Processing and Extractive Metallurgy Review* **5**, 43 (1989).
 - [5] J. Finch and G. Dobby, Column flotation (Pergamon Press, Oxford, 1990).
 - [6] B. Albijanic, O. Ozdemir, A. V. Nguyen, and D. Bradshaw, *Advances in colloid and interface science* **159**, 1 (2010).
 - [7] Z. Wang and J. Zhe, *Lab on a Chip* **11**, 1280 (2011).
 - [8] Y. Chen and S. Lee, *Integrative and comparative biology* **54**, 959 (2014).
 - [9] P. Marmottant, M. Versluis, N. de Jong, S. Hilgenfeldt, and D. Lohse, *Experiments in Fluids* **41**, 147 (2005).
 - [10] Y. Chen, Z. Fang, B. Merritt, D. Strack, J. Xu, and S. Lee, *Lab on a Chip* (2016).
 - [11] W. Eck and J. Siekmann, *Ingenieur-Archiv* **47**, 153 (1978).
 - [12] A. R. Kopf-Sill and G. M. Homsy, *Physics of Fluids* **31**, 18 (1988).
 - [13] S. R. K. Maruvada and C.-W. Park, *Physics of Fluids* **8**, 3229 (1996).
 - [14] T. Maxworthy, *Journal of Fluid Mechanics* **173**, 95 (1986).
 - [15] C.-W. Park, S. Gorell, and G. M. Homsy, *Journal of Fluid Mechanics* **141**, 275 (1984).
 - [16] P. G. Saffman, *Journal of Fluid Mechanics* **173**, 73 (1986).
 - [17] C. Pozrikidis, *Journal of Fluid Mechanics* **210**, 1 (1990).
 - [18] H. A. Stone, B. J. Bentley, and L. G. Leal, *Journal of Fluid Mechanics* **173**, 131 (1986).
 - [19] D. R. Link, S. L. Anna, D. A. Weitz, and H. A. Stone, *Physical Review Letters* **92**, 054503 (2004).
 - [20] S. Protière, M. Z. Bazant, D. A. Weitz, and H. A. Stone, *EPL (Europhysics Letters)* **92** (2010).
 - [21] S. A. Vanapalli, M. H. G. Duits, and F. Mugele, *Biomicrofluidics* **3**, 012006 (2009).
 - [22] L. Salkin, L. Courbin, and P. Panizza, *Physical Review E* **86**, 036317 (2012).
 - [23] L. Salkin, A. Schmit, L. Courbin, and P. Panizza, *Lab on a Chip* **13**, 3022 (2013).
 - [24] See Supplemental Material at [] for three representative motions of the bubble.
 - [25] C. H. Reinsch, *Numerische mathematik* **10**, 177 (1967).

[26] A. Eri and K. Okumura, *Soft Matter* **7**, 5648 (2011).

[27] R. Danga, S. Lee, and C. N. Baroud, *Physical Review Letters* **107**, 124501 (2011).